Tissue tectonics: morphogenetic strain rates, cell shape change and intercalation

Guy B Blanchard[1], Alexandre J Kabla[2], Nora L Schultz[1], Lucy C Butler[1], Benedicte Sanson[1], Nicole Gorfinkiel[3], L Mahadevan[4,5] & Richard J Adams[1]

The dynamic reshaping of tissues during morphogenesis results from a combination of individual cell behaviors and collective cell rearrangements. However, a comprehensive framework to unambiguously measure and link cell behavior to tissue morphogenesis is lacking. Here we introduce such a kinematic framework, bridging cell and tissue behaviors at an intermediate, mesoscopic, level of cell clusters or domains. By measuring domain deformation in terms of the relative motion of cell positions and the evolution of their shapes, we characterized the basic invariant quantities that measure fundamental classes of cell behavior, namely tensorial rates of cell shape change and cell intercalation. In doing so we introduce an explicit definition of cell intercalation as a continuous process. We mapped strain rates spatiotemporally in three models of tissue morphogenesis, gaining insight into morphogenetic mechanisms. Our quantitative approach has broad relevance for the precise characterization and comparison of morphogenetic phenotypes.

One of the most important challenges in developmental biology is to understand how molecular information leads to the individual and collective movement of cells that shape and form tissues[1–4] via both cell-intrinsic stresses and cell responses to applied stress[5–7]. With the tremendous advances in molecular biology, genetics, imaging techniques and the automated tracking of many cells in parallel[8,9], it is now possible to trace the evolution of morphogenetic phenotypes during development as a function of molecular perturbations as well as physical manipulation. This sets the stage for the identification and quantification of the geometry of shape change in terms of the resultant strain (deformation) rates, that is, the amount of strain per unit of time (a glossary of the most commonly used terms are listed in **Supplementary Note 1** online). The response of tissues to the sum of the external and cell-autonomous forces, constraints and stiffnesses is characterized by tissue strains and strain rates.

Current approaches to the statistical characterization of morphogenetic parameters rely on analogies of tissues to foams and granular materials, where topological methods that rely on connectivity are used[10]. Here we used ideas from tensor analysis and continuum field theories[11] and extended these methods for tissues composed of discrete cells to measure strain rates and rotations in biological tissues. This allowed us to account for the continuous sliding process between cells regardless of their connectivity. In particular, we quantified the rates of individual cell shape change and collective cell intercalation (cell rearrangement), the two fundamental classes of mesoscopic cellular behavior, combinations of which account for a wide range of tissue shaping behaviors. Cell shape change and cell intercalation can be active cell-autonomous behaviors, and also possibly passive deformations (elastic or plastic) in response to external forces or constraints. Patterns of strain rates allow modeling of the forces acting on and within tissues and reveal signatures of active and passive behavior.

We used these measures on a variety of simulated and real deforming tissues, building dynamic maps of morphogenetic behavior. We could determine the relative contribution of these two behaviors in shaping tissues. First, the *Drosophila melanogaster* amnioserosa deformed predominantly by cell shape change during dorsal closure, and we found that there was little cell intercalation. Second, during mid-phase *Drosophila* germband extension we resolved and distinguished different cellular modes underlying tissue extension. Lateral ectoderm extended by cell intercalation whereas ventral midline cells extended by stretching, without intercalation. Third, in the zebrafish trunk neuroectoderm, intercalation and cell shape change combined in an interesting way, the latter augmenting tissue convergence and reducing tissue extension. By following cell behavior and coupling these to global movements of cellular domains we laid out a high-resolution quantitative framework for the geometric basis of morphogenesis.

RESULTS

Tissue strain rates

Computer-assisted cell tracking allowed us to follow the behaviors of many epithelial cells within two-dimensional surfaces that follow the shape of tissues within the embryo (Online Methods and **Supplementary Videos 1–3** online). Morphogenetic deformations
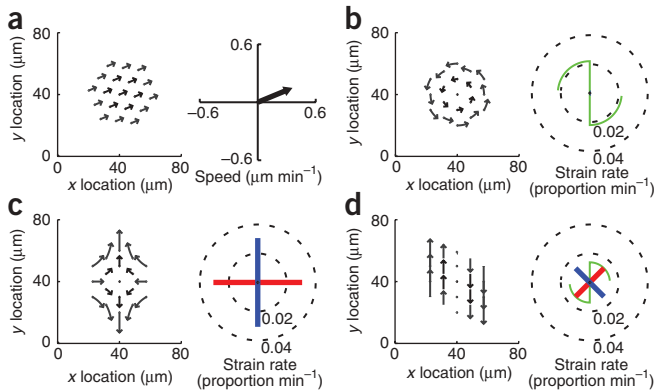
Figure 1 | Measuring tissue strain rates in simulated data. (**a**–**d**) Trajectories (left) and either domain translation (**a**) or tissue strain rates (**b**–**d**) (right) for simulated domains (number of coronae, $n_c = 2$; and time interval, $dt = 9$ min). Principal strain rates are represented by orthogonal line segments with length equal to strain rate amplitude (blue, positive and red, negative). Rotation is represented by a green scythe motif, with radius indicating radians per minute on the same scale as the strain rates. Blades point in the direction of rotation (anticlockwise in **b** and clockwise in **d**). The domain behaves as a rigid block translating with velocities uniform within the domain (**a**). Pure rotation (**b**). Balanced convergence and extension, or pure shear (**c**). An equal combination of pure shear and rotation, or simple shear (**d**).

result from variation in the speed or direction of cell trajectories that change the relative positions of cells[8]. To quantify deformations at a multicellular scale, we followed, over a short time interval (minutes), small groups of cells or domains. We defined domains by a central cell and a small number of coronae of neighboring cells at the central time point.

We treated each domain as a continuous field of tissue sampled at cell centroid locations and calculated various domain metrics based on the movement of these centroids (Online Methods). First, we calculated the average domain translation velocity, how fast the domain moves in space (**Fig. 1a**). Second, we calculated gradients of centroid velocities across the domain in two orthogonal orientations and used these gradients to construct a tissue velocity gradient tensor, $\mathbf{L_T}$, which characterizes the spatial variation of the local velocity field. We then separated $\mathbf{L_T}$ into a spin matrix, $\mathbf{\Omega_T}$, which yields the domain rotation (angular velocity) in radians per minute (**Fig. 1b**) and a deformation or strain rate tensor, $\mathbf{\dot{E}_T}$. An invariant description of domain strain rates (that is, one that is independent of the chosen coordinate system) is given by the eigenvalues and associated eigenvectors of $\mathbf{\dot{E}_T}$. These are the amplitudes (in proportion per minute) and orientations of the local principal strain rates associated with the velocity field (**Fig. 1c**). The eigenvalues of $\mathbf{\dot{E}_T}$ generalize the local convergence (negative) and extension (positive) rate constants previously described[12].

Domain translation and rotation measure how the domain moves as a whole in space, and the strain rate tensor measures how the domain itself deforms, that is, how distances and angles between cells vary locally. The rotation component nevertheless remains important for interpreting simple classes of local deformations. For instance, simple shear arises from a combination of rotation and a pure shear deformation (**Supplementary Note 1** and **Fig. 1d**). However, a mechanistic interpretation remains ambiguous at the level of the single domain because it is not possible to distinguish between local rotation that is (i) due to an advective motion resulting from activity extraneous to the domain or because of embryo movement and (ii) part of a simple shear deformation.

Cell shape and cell intercalation strain rates
To interpret tissue deformation in terms of the intrinsic cell behavior within each domain, we identified two complementary components: cell shape change and cell intercalation. We illustrated their distinction with two simulated scenarios (**Supplementary Videos 4** and **5** online) wherein tissue convergence and extension were equal but were accounted for by cell shape change or cell

intercalation, respectively (**Fig. 2a,b**). In another example, mutually cancelling cell shape change and intercalation resulted in no tissue deformation (**Fig. 2c**). *In vivo*, we expected morphogenesis to involve combinations of cell shape change and cell intercalation that differ with tissue, time and location. We estimated a cell shape strain rate tensor, $\mathbf{L_C}$, from traced cell outlines based on their best-fit ellipses (Online Methods). We assumed that average cell spin, $\mathbf{\Omega_C}$, equals $\mathbf{\Omega_T}$, that is, cells rotate only with the domain. We therefore eliminated the effects of the rotation $\mathbf{\Omega_T}$ before calculating a symmetrical cell shape strain rate tensor, $\mathbf{\dot{E}_C}$, which represented the average rate of change in the shape of cells within a domain. The average rate of change in cell area is given by the trace of $\mathbf{\dot{E}_C}$ as a result of movement of cell volume into or out of the plane[13].

To characterize cell intercalation in terms of these tensorial quantities, we proposed that the principal characteristic of cell intercalation is the continuous sliding of the bulk of neighboring cells past each other. We found that the local rate and principal directions of sliding derive directly from what we call the cell intercalation strain rate tensor, $\mathbf{L_I}$, defined by:

$$\mathbf{L_I} = \mathbf{L_T} - \mathbf{L_C} \tag{1}$$

(Online Methods and **Supplementary Fig. 1** online). As one would expect, $\mathbf{L_I}$ is intimately related with the mismatch between the cell shape and tissue strain rates. This explicitly defines cell intercalation as a measure that bridges spatial scales: it represents the residual difference in bulk movement between $\mathbf{L_T}$, the redistribution of the bulk of the domain relative to its center, and $\mathbf{L_C}$, the average redistribution of each cell's bulk relative to its own centroid. As both $\mathbf{L_C}$ and $\mathbf{L_T}$ capture the change in area of the cells in the domain (volume change in three dimensions), $\mathbf{L_I}$ has zero dilatation and is a pure shear deformation. This definition is valid in both two and three dimensions. Thus intercalation is a process in which convergence rate in one orientation is balanced by an equal rate of extension in the orthogonal orientation: it preserves area (in two dimensions) and volume (in three dimensions).

To get an intuitive understanding of this simple measure, we applied our methods to simulated data. In our first example, net cell shape strain was identical to tissue strain, and there was no cell intercalation (**Fig. 2d–f**). In the second example, cell intercalation accounted for virtually all of the tissue strain (**Fig. 2g–i**) and was continuous, unlike the synchronous and discrete neighbor-exchange events (**Supplementary Video 5**). Net cell shape strain was minimal, fluctuating owing to transient packing changes required in the T1 neighbor exchange process[14], as in biological tissues undergoing cell intercalation[2,12]. In our third example, there was zero tissue strain, and dramatic cell shape strain was balanced by intercalation strain in opposite orientations (**Fig. 2j–l**). These
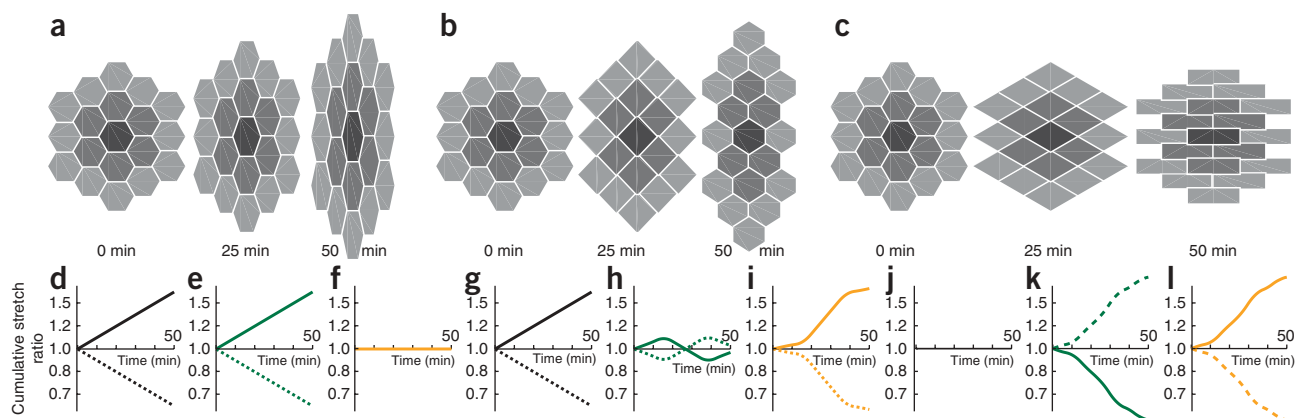
Figure 2 | Cellular simulations of tissue morphogenesis. (**a–c**) Simulations of three cellular scenarios, demonstrating tissue outcomes for different combinations of cell shape change and cell intercalation. Focal cell is black, with first and second coronae of neighboring cells in dark and light gray, respectively. (**d–l**) Cumulative stretch ratios on a log scale versus time for examples in **a** (**d–f**), **b** (**g–i**) and **c** (**j–l**). Cumulative stretch ratios in vertical (solid) and horizontal (dotted) orientations are plotted for tissue (**d,g,j**) in black, cell shape (**e,h,k**) in dark green and cell intercalation (**f,i,l**) in orange.

examples highlight the differences between our continuous measures based on cell shape measurements and topological measures which are based on discrete changes in cell-cell connectivity[8,15,16]. We consider the more fundamental and continuous sliding process that our methods capture, regardless of cell topology, to be better suited to precise spatiotemporal mapping. In each of these examples, we could track four related measures; cell shape, cell intercalation and tissue strain rates, and the tissue rotation rate.

We used these measures to quantify convergence and extension in a single example domain of zebrafish trunk neuroectoderm (**Fig. 3**). Tissue strain rates (**Fig. 3e**) showed that the domain exhibited unequal convergence and extension, with extension oriented close to the anterior-posterior (AP) axis. A clockwise rotation, of similar magnitude to the strain rates, shows that a simple shear has taken place. Both cell shape change (**Fig. 3g**) and cell intercalation (**Fig. 3h**) contribute to the net domain deformation, with the convergence orientation of intercalation aligned with the orientation of cell shape contraction. We also calculated confidence intervals associated with each strain rate and used these to establish an appropriate domain size for a tissue (Online Methods and **Supplementary Fig. 2** online). An outline of the sequence of algorithms used to calculate strain rates from four-dimensional movies of tissues with membranes marked with ubiquitous fluorescence is available (**Supplementary Fig. 3** online), and full code for calculating strain rates and associated information for a domain of cells is available (**Supplementary Software** online).
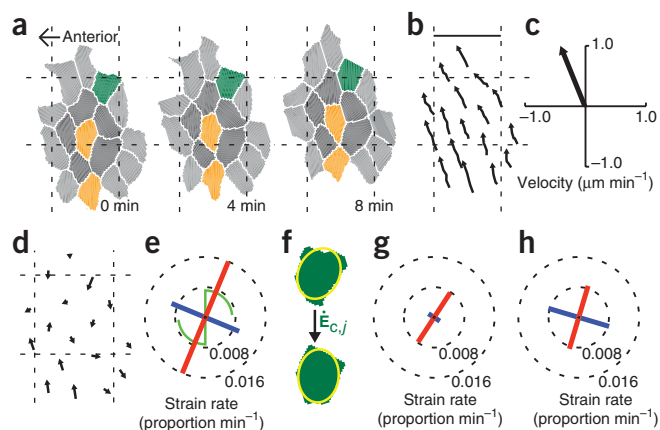
Biological applications

We quantitatively mapped the morphogenesis of three diverse embryonic epithelial tissues in which we expected different combinations of cell shape change and intercalation. To create maps of developing tissues, we calculated strain rates for domains surrounding each cell and for each time point. We averaged summary measures of strain rates over space and integrated them over time from average or cumulative tensors, respectively. In all three tissues, the dominant orientations of deformation were strongly aligned with the body axes, so we present cumulative stretch ratios (the exponent of the cumulative strains) projected onto these axes.

Drosophila amnioserosa

The *Drosophila* amnioserosa is an ectodermal tissue eclipsed by the dorsal closure of lateral epidermis[17] (**Fig. 4a** and **Supplementary Video 1**). The forces acting at the tissue margins are well understood[5] and the amnioserosa tissue is thought to contract actively in the medio-lateral (ML) orientation[18,19]. However, little is known about the behavior of individual cells during this process. Tissue deformation had strong ML direction–oriented convergence across the tissue but also some weaker AP direction–oriented convergence (**Fig. 4b–d** and **Supplementary Video 6** online). Highly

Figure 3 | Measuring strain rates for a domain of zebrafish neuroectoderm. (**a,b**) Cell shapes (**a**) and cell centroid trajectories (**b**) for a domain ($n_c = 2$, $dt = 4$ min) used to calculate strain rates. Cell colors in **a** show first (dark gray) and second (light gray) coronae of neighbors around the focal central cell, with examples of cell shape change (dark green) and intercalation (orange). Scale bar, 25 μm (**b**). (**c**) Average domain translation velocity. (**d**) Velocity field. (**e**) Tissue strain and rotation rates. Strain rate line segments and rotation rates are drawn as in **Figure 1**. (**f**) Cell shapes are approximated to their best-fit ellipses (yellow) and strain rates that must be applied to account for a cell's shape evolution from time $t - dt$ to $t + dt$ are calculated for all cells (j) of the domain. (**g**) Area-weighted average cell shape strain rates. (**h**) Cell intercalation strain rates.

asymmetric tissue deformation resulted almost exclusively from equally asymmetric cell shape changes, by narrowing cells

predominantly in the ML orientation at a rate that accelerated with time (**Fig. 4b,e,f** and **Supplementary Video 7** online). Cells
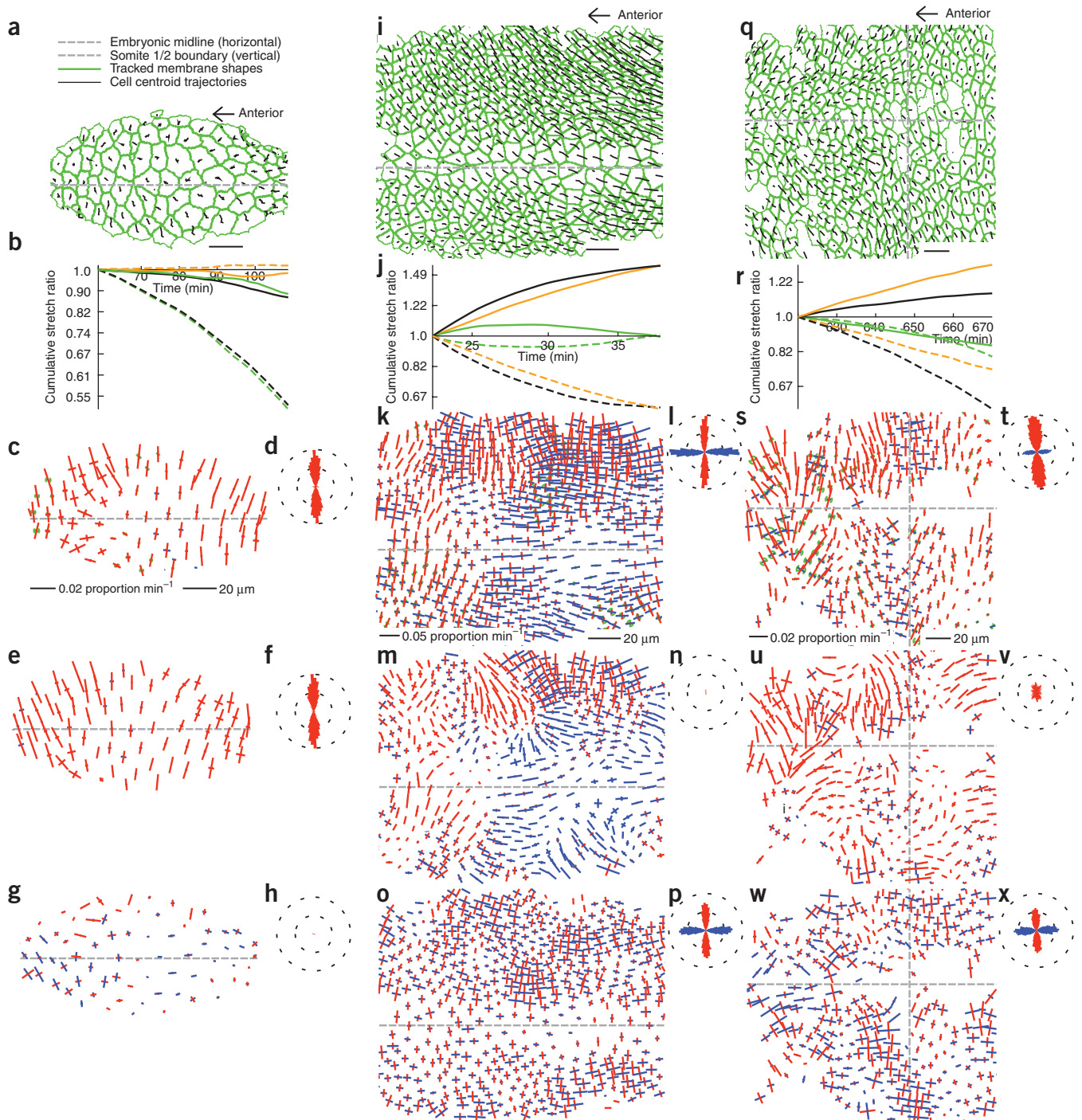
Figure 4 | Tissue, cell shape and intercalation strain rate patterns in *Drosophila* and zebrafish ectoderm. (**a–h**) *Drosophila* amnioserosa midway through dorsal closure (time is from the start of dorsal closure in **b**). (**i–p**) *Drosophila* germband midway through germband extension (time is from the start of germband extension in **j**), with the left margin of the field of view approximately four cell diameters posterior to the cephalic furrow. (**q–x**) Zebrafish trunk neuroectoderm just before the onset of neurulation, starting at 620 min after fertilization. Selected tracked cell trajectories and cell shapes within curved layers taken through the apices of the three epithelial tissues imaged by three-dimensional time-lapse confocal microscopy (**a,i,q**; scale bars, 20 μm). Gaps in **q** indicate tracking ambiguities. Cumulative stretch ratios (**b,j,r**), integrated across AP (solid) and ML (dotted) orientations for total tissue (black), cell shape (green), and cell intercalation (orange), plotted as in **Figure 2**. Tissue strain rates for domains centered on each cell for a single time point (**c,k,s**). Colors of strain rates and rotations are as in **Figure 1**. Radial histograms (left-right is AP) of whole movie pooled tissue strain rate orientations, weighted by their absolute magnitude (**d,l,t**). Orientations with positive (expansive) mean strain rates are blue, negative (contractile) red. Cell shape (**e,m,u**) and cell intercalation strain rates (**g,o,w**) for domains centered on each cell, for the same time point as shown for tissue strain rates, with associated strain rate orientation histograms (**f,n,v** and **h,p,x**, respectively) are drawn as for tissue strain rates.
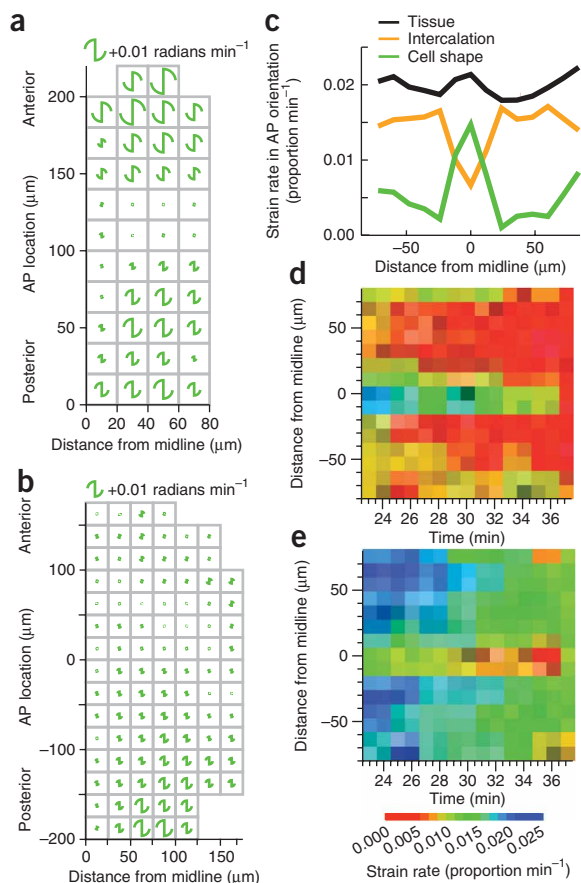
Figure 5 | Patterns in data pooled from multiple embryos. (**a,b**) Pooled rotation data from multiple embryos, summarized for squares of tissue for *Drosophila* germband (averaged over 5–20 min after the start of germband extension; **a**) and zebrafish trunk ectoderm (averaged over 560–610 min after fertilization; **b**). Data for the left half of each embryo have been mirrored onto the right side. AP location of ~220 μm is the cephalic furrow in **a** and of 0 μm is the somite 1/2 boundary in **b**. (**c–e**) Pooled average strain rates from 5 wild-type *Drosophila* embryos, projected onto the AP (extension) axis for the epoch of mid-germband extension shown in **Figure 4j**. Time is from the start of germ-band extension. Average cell shape (**d**) and intercalation (**e**) strain rates.

contracted to nearly 50% of their original ML size (average −0.013 pp min⁻¹) and to 88% of their AP size in the mid-zippering phase of dorsal closure analyzed. There was only weak and late cell intercalation that summed to a minor net contribution (**Fig. 4b,g,h** and **Supplementary Video 8** online).

Drosophila germband

The *Drosophila* post-gastrulation germband extends to the posterior as cells converge toward the ventral midline[2,20,21] (**Fig. 4i** and **Supplementary Video 2**). Cell intercalation is known to contribute to this process but how much this alone can account for tissue deformation is unknown. In the mid-phase, strong tissue convergence in the ML direction was matched by extension in the AP direction (**Fig. 4j,k,l** and **Supplementary Video 9** online). In contrast to the amnioserosa, strong cell shape changes were heterogeneous across the tissue and canceled to give minimal net contribution over time (**Fig. 4j,m,n** and **Supplementary Video 10** online). Ectodermal tissue deformation was predominantly due to strong cell intercalation co-oriented with the body axes (**Fig. 4j,m,n** and **Supplementary Video 11** online). Additional analysis of cell shape changes is presented elsewhere[22].

Zebrafish trunk neuroectoderm

Zebrafish trunk neural ectoderm converges in the ML orientation while extending along the AP axis, before and during neurulation[3,23] (**Fig. 4q** and **Supplementary Video 3**). The temporal and spatial contributions of cell intercalation and cell shape change in the neural plate are poorly understood[3,24]. The neural plate had strong convergence in tissue strain rate in the ML orientation but

heterogeneous AP axis extension (**Fig. 4r,s,t** and **Supplementary Video 12** online). The rate of tissue deformation increased over time, but AP direction–oriented extension never matched ML direction–oriented convergence. Cell shape strain rate within the neural plate was mostly negative (**Fig. 4r,u,v** and **Supplementary Video 13** online), both in ML and AP orientations, as cells became smaller in the plane and lengthened in depth. Notably, cell intercalation across the tissue was strongly aligned with the body axes (**Fig. 4r,w,x** and **Supplementary Video 14** online). The average magnitude of cell shape change was about half that of cell intercalation. We can now correctly interpret the imbalance between tissue convergence and tissue extension: the combination of cell shape change and cell intercalation were additive in the ML orientation but cancelled in the AP orientation.

Tissue rotation

We measured average tissue rotation rates for the *Drosophila* germband for data pooled from 5 embryos (Online Methods) during the fast phase of germband extension. The rotation rate varied from clockwise anterior (for the right ventral ectoderm) to anticlockwise in the posterior, with little rotation in between (**Fig. 5a**). Similarly, in the zebrafish trunk, there was a gradient of the rotation rate along the AP axis (**Fig. 5b**) in data pooled from 9 embryos.

Domain variability

The high spatiotemporal resolution of our approach allowed us to detect local variation in cell behavior. The patterns of cell shape change and the strength of intercalation, in particular in the germband and zebrafish trunk, were remarkably complex in space (**Fig. 4m,o,u,w**) and in time (**Supplementary Videos 10, 11, 13** and **14**), presumably reflecting variation in combinations of gene expression, cell signaling, cell-intrinsic fluctuations, local stresses[21] and physical constraints. For cell shape change in the amnioserosa and intercalation in the germband and zebrafish trunk, the orientations of domain deformation were aligned predominantly with the body axes (**Fig. 4f,p,x**). The orientation of intercalation is correlated with cell polarization in the germband[1] and the zebrafish trunk[20], with characteristic average rates of ~0.03 proportion min⁻¹ and ~0.006 proportion min⁻¹, respectively. We identified a consistent spatial heterogeneity during germband extension, along a narrow band of cells at the ventral midline, so we explored the ventral midline of *Drosophila* and the dorsal midline of zebrafish using data pooled from several embryos (Online Methods). In the germband, although AP direction–oriented tissue extension was constant along the ML axis (**Fig. 5c**), cell shape change was weak laterally but strong along the ventral midline (**Fig. 5d**). Conversely, cell intercalation was

strong laterally but weak medially (**Fig. 5e**). A 15 μm region on either side of the ventral midline comprised two lines of ventral midline neural precursor (VML) cells. Thus, during germband extension the VML cells extended in the AP orientation not by intercalation but by shape stretch, whereas the lateral cells intercalated. The same analysis of the dorsal midline of zebrafish embryos showed that there was no such inversion of cellular mechanisms at the midline of the fish trunk neuroectoderm at ∼10–11 h after fertilization (**Supplementary Fig. 4** online). Indeed, at this pre-neurulation stage, intercalation is strong across the midline.

DISCUSSION

Our quantitative measurements went well beyond qualitative comparisons of dominant behaviors in three example tissues and revealed detailed spatial and temporal patterns in morphogenetic processes. We identified new and specific features in each tissue. Cell intercalation in the *Drosophila* amnioserosa made only a weak contribution to late dorsal closure. We observed cell shape contraction in the AP orientation, in addition to the stronger ML-direction contraction, which suggests that isometric apical contraction encounters greater resistance to deformation in AP orientation, as amnioserosa cells are not known to be polarized[25]. Additional investigation of the dynamics in dorsal closure mutants will help elucidate the relative contribution of the various forces and constraints[26]. In the *Drosophila* germband, but not in the zebrafish trunk, there was an inversion of mechanisms at the midline, with VML cells undergoing cell shape extension in the AP direction, whereas the lateral ectoderm extended by intercalation. A mechanistic understanding of intercalation in the germband must therefore explain why there is no intercalation across the midline and how the lateral ectoderm cells can make new connections with but not through VML cells. In the zebrafish trunk, cell shapes contracted in the AP and ML directions as cells elongated in depth, reducing tissue AP extension and augmenting ML convergence. Our strain breakdown clarified the planar combinations that are possible. Cell intercalation is by definition balanced orthogonal convergence and extension. It is only the addition of unbalanced cell shape (that is, when there is a change in area) that leads to an imbalance in tissue convergence and extension.

The rotation measure, in addition to the tissue deformation field, provides a key component to test mechanical models of tissue tectonics, as used in plate tectonics[27]. Such patterns signify deformation gradients, here predominantly owing to an increasing rate of AP extension toward the midline in both the germband[22] and the zebrafish trunk (N.L.S., G.B.B., A.J.K., L.M. & R.J.A.; manuscript in preparation). Where intercalation and rotation happen together, two interpretations are possible. If the tissue rotation is a result of cell rotation, then the tissue rotation is not associated with slippage. However, if there is no cell rotation then a new type of behavior, intercalation simple shear, is identified, in which lines of fracture are a result of slippage in one orientation only. However, we cannot currently unambiguously separate intercalation rotation from cell shape rotation, so future analysis of the shear structure and planes of shear at the cellular and subcellular scale will provide insights about the cellular organization of tissues.

Our biological examples confirmed that two fundamental and complementary classes of cellular events can now be faithfully distinguished and exquisite patterns revealed. Our quantitative approaches allow us to assay morphogenetic phenotypes with unprecedented detail and rigor and facilitate comparisons between individuals, manipulations, genotypes and species to probe the variability of developmental programs. We suspect that many genetic phenotypes are being missed or misinterpreted through lack of suitable methods and because similar final phenotypes can be achieved through different developmental mechanisms. An immediate application of our methods is therefore quantitative phenotypic screening based on comparisons of rates of cell shape change and intercalation.

METHODS

Methods and any associated references are available in the online version of the paper at http://www.nature.com/naturemethods/.

Note: Supplementary information is available on the Nature Methods website.

AUTHOR CONTRIBUTIONS
G.B.B., A.J.K., L.M. and R.J.A. conceived and developed the project and wrote the manuscript. G.B.B. and A.J.K. analyzed data and developed the code. N.L.S. (zebrafish trunk), L.C.B., B.S. (*Drosophila* germband extension) and N.G. (*Drosophila* dorsal closure) all collaborated to develop the analyses and contributed time-lapse movies and expertise on their models.

1. Keller, R. *et al.* Mechanisms of convergence and extension by cell intercalation. *Phil. Trans. Roy. Soc. B* **355**, 897–922 (2000).
2. Bertet, C., Sulak, L. & Lecuit, T. Myosin-dependent junction remodelling controls planar cell intercalation and axis elongation. *Nature* **429**, 667–671 (2004).
3. Concha, M.L. & Adams, R.J. Oriented cell divisions and cellular morphogenesis in the zebrafish gastrula and neurula: a time-lapse analysis. *Development* **125**, 983–994 (1998).
4. Neumann, M. & Affolter, M. Remodelling epithelial tubes through cell rearrangements: from cells to molecules. *EMBO Rep.* **7**, 36–40 (2006).
5. Hutson, M.S. *et al.* Forces for morphogenesis investigated with laser microsurgery and quantitative modelling. *Science* **300**, 145–149 (2003).
6. Moore, S.W., Keller, R.E. & Koehl, M.A.R. The dorsal involuting marginal zone stiffens anisotropically during its convergent extension in the gastrula of *Xenopus laevis*. *Development* **121**, 3131–3140 (1995).
7. Keller, R., Shook, D. & Skogland, P. The forces that shape embryos: physical aspects of convergent extension by cell intercalation. *Phys. Biol.* **5**, 15007 (2008).
8. England, S.J., Blanchard, G.B., Mahadevan, L. & Adams, R.J. A dynamic fate map of the forebrain shows how vertebrate eyes form and explains two causes of cyclopia. *Development* **133**, 4613–4617 (2006).
9. Keller, P.J., Schmidt, A.D., Wittbrodt, J. & Stelzer, E.H.K. Reconstruction of zebrafish early embryonic development by scanned light sheet microscopy. *Science* **322**, 1065–1069 (2008).
10. Graner, F., Dollet, B., Raufaste, C. & Marmottant, P. Discrete rearranging disordered patterns, part I: Robust statistical tools in two or three dimensions. *Eur. Phys. J. E* **25**, 349–369 (2008).
11. Fung, Y.C. & Tong, P. *Classical and Computational Solid Mechanics* (World Scientific, Singapore, 2001).

12. Glickman, N.S., Kimmel, C.B., Jones, M.A. & Adams, R.J. Shaping the zebrafish notochord. *Development* **130**, 873–887 (2003).
13. Yin, C. *et al.* Cooperation of polarized cell intercalations drives convergence and extension of presomitic mesoderm during zebrafish gastrulation. *J. Cell Biol.* **180**, 221–232 (2008).
14. Weaire, D. & Hutzler, S. *The Physics of Foams* (Oxford University Press, Oxford, 2001).
15. Farhadifar, R. *et al.* The influence of cell mechanics, cell-cell interactions, and proliferation on epithelial packing. *Curr. Biol.* **17**, 2095–2104 (2007).
16. Hilgenfeldt, S., Erisken, S. & Carthew, R.W. Physical modeling of cell geometric order in an epithelial tissue. *Proc. Natl. Acad. Sci. USA* **105**, 907–911 (2008).
17. Jacinto, A., Woolner, S. & Martin, P. Dynamic analysis of dorsal closure in *Drosophila*: from genetics to cell biology. *Dev. Cell* **3**, 9–19 (2002).
18. Kiehart, D.P. *et al.* Multiple forces contribute to cell sheet morphogenesis for dorsal closure in *Drosophila*. *J. Cell Biol.* **149**, 471–490 (2000).
19. Fernandez, B.G., Arias, A.M. & Jacinto, A. Dpp signalling orchestrates dorsal closure by regulating cell shape changes both in the amnioserosa and in the epidermis. *Mech. Dev.* **124**, 884–897 (2007).
20. Irvine, K.D. & Weischaus, E. Cell intercalation during *Drosophila* germband extension and its regulation by pair-rule segmentation genes. *Development* **120**, 827–841 (1994).
21. Blankenship, J.T. *et al.* Multicellular rosette formation links planar cell polarity to tissue morphogenesis. *Dev. Cell* **11**, 459–470 (2006).
22. Butler, L.C. *et al.* Cell shape changes indicate a role for extrinsic tensile forces in *Drosophila* germband extension. *Nat. Cell Biol.* (in the press).
23. Keller, R., Shih, J. & Sater, A. The cellular basis of the convergence and extension of the *Xenopus* neural plate. *Dev. Dyn.* **193**, 199–217 (1992).
24. Hong, E. & Brewster, R. N-cadherin is required for the polarized cell behaviors that drive neurulation in the zebrafish. *Development* **133**, 3895–3905 (2006).
25. Pope, K.L. & Harris, T.J. Control of cell flattening and junctional remodelling during squamous epithelial morphogenesis in *Drosophila*. *Development* **135**, 2227–2238 (2008).
26. Gorfinkiel, N., Blanchard, G.B., Adams, R.J. & Arias, A.M. Mechanical control of global cell behaviour during dorsal closure in *Drosophila*. *Development* (in the press).
27. Allmendinger, R.W., Relinger, R. & Loveless, J. Strain and rotation rate from GPS in Tibet, Anatolia, and the Altiplano. *Tectonics* **26**, TC3013 (2007).

ONLINE METHODS

Tissue strain rate. For each cell j in a domain in plane x,y, we calculated its location, $\mathbf{r}_j$ (x_j,y_j), and its velocity, $\mathbf{u}_j$ (u_j,v_j component velocities in x and y directions, respectively). We used domains of $n_c = 1$–3 coronae, which were sufficiently small to be treated as flat planes, once corrected for surface tilt. The local velocity field could therefore be treated as linear and a planar regression was used to characterize the domain behavior in terms of the local strain rates using the form:

$$u_j \approx\; <u> + \partial u/\partial x\, x_j + \partial u/\partial y\, y_j \qquad (2)$$

$$v_j \approx\; <v> + \partial v/\partial x\, x_j + \partial v/\partial y\, y_j \qquad (3)$$

which can be written in matrix notation as:

$$\mathbf{u}_j \approx\; <\mathbf{u}> + \mathbf{L_T}\, \mathbf{r}_j \qquad (4)$$

$$\text{with } \mathbf{L_T} = \begin{vmatrix} \partial u/\partial x & \partial u/\partial y \\ \partial v/\partial x & \partial v/\partial y \end{vmatrix}$$

Here the average domain translation velocity is $<\mathbf{u}>$ and the tissue velocity gradient tensor is $\mathbf{L_T}$. We chose the time interval dt such that the tissue domain deformation was small (each coefficient of $\mathbf{L_T} < 0.1$), which permitted a simple decomposition of $\mathbf{L_T}$ into an antisymmetric spin $\mathbf{\Omega_T} = (\mathbf{L_T} - \mathbf{L_T}^T)\,/\,2$, and a symmetric strain rate tensor, $\dot{\mathbf{E}}_T = (\mathbf{L_T} + \mathbf{L_T}^T)\,/\,2$. The trace of $\mathbf{L_T}$ ($=$ trace $\dot{\mathbf{E}}_T$) gives the rate of change in area of the domain.

Cell shape strain rate. Without independent fiducial (registration) marks within or around cells that can be followed over time, cell rotation could not be determined unambiguously. Movements of individual vertices at the junctions between cells have no direct relationship with the overall changes in cell shape; the latter would therefore not be properly measured by registration methods that track details of the cell contour. We instead used the traced outlines of tracked cells to extract a statistical representation of their deformation. We found the deformation that minimises the squared area difference between the starting cell shape, deformed by the estimated $\dot{\mathbf{E}}_{C,j}$, and the final cell shape. Trace $\dot{\mathbf{E}}_{C,j}$ was constrained to be $\ln(\text{area}_{(t+dt),\,j}\,/\,\text{area}_{(t-dt),\,j}\,/\,2dt)$ to conserve area change. Eigenvector and eigenvalue space was searched for the optimal $\dot{\mathbf{E}}_{C,j}$ using the Nelder-Mead minimization method[28]. $\dot{\mathbf{E}}_C$ was then the area-weighted average of $\dot{\mathbf{E}}_{C,j}$ for all cells of the domain. In practice, we found that simplifying real cell shapes to their best-fit ellipses dramatically sped up calculations with minimal change to the resulting $\dot{\mathbf{E}}_C$ values. The fit of an ellipse (**Fig. 3f**) to a cell shape was optimized by maximizing the area overlap, with the area of the ellipse constrained to be identical to that of the cell shape. An alternative approach, that was not developed here, is to use methods derived from the statistical strain tensors[29].

Intercalation strain rate. $\mathbf{L_T}$ characterizes the relative velocities of cell centroids and $\mathbf{L_C}$ represents the average redistribution of each cell's bulk relative to its centroid, that is, the relative velocities of points within a cell. Any mismatch between them can be conveniently represented by a slippage velocity. We use slippage in an abstract sense of a relative movement of cell bulk without being explicit about what biological mechanism mediates this at the interfaces between cells. Consider a point P located between two neighboring cells 1 and 2 (**Supplementary Fig. 1**). We estimated the displacement of this point with respect to the center of cell 1; we obtained $\mathbf{v}_1 = \mathbf{L_C}\mathbf{r}_{1p}$. Similarly, for cell 2, $\mathbf{v}_2 = \mathbf{L_C}\mathbf{r}_{2p}$, and the center of cell 2 moved at a speed $\mathbf{v}_{1,2} = \mathbf{L_T}\mathbf{r}_{1,2}$. The local rate of slippage on the point P is then:

$$\mathbf{v}_s = \mathbf{v}_{1,2} + \mathbf{v}_2 - \mathbf{v}_1 = (\mathbf{L_T} - \mathbf{L_C})\mathbf{r}_{1,2} = \mathbf{L_I}\mathbf{r}_{1,2}$$
$$\text{with } \mathbf{L_I} = \mathbf{L_T} - \mathbf{L_C}.$$

This construction shows that the knowledge of the displacement and shape change of two cells is a priori sufficient to give an estimate of the continuous process of planar intercalation. Our general method provided the averaging required for accurate and robust measurements at the mesoscopic scale.

Strain rate errors. Practical considerations in calculating tissue deformations and spins include the choice of domain size and time interval, the requirements for which may vary between tissues. We measured the consensus tissue deformation in each domain using regression to minimize residual cell centroid movement (equations 2 and 3). The sources and magnitudes of residuals will depend both on cell behavior inhomogeneity and measurement error. Biological sources of inhomogeneity include nonlinear patterns of behavior within domains, domains spanning boundaries between differing tissues or behaviors and nonuniform cell behavior, such as cell division or isolated cells moving into or from the plane. In these analyses, we treated a cell going through cell division as one cell for the duration of a domain even if it split fully into daughters, and hence this was measured as a cell shape change. Measurement errors arose from noise due to pixelation of cell shapes and remaining errors in cell-tracking. It is difficult to tease apart these potential sources so we combined them into a total domain error, e. Irrespective of its source, we wanted to be able to quantify the error and relate it to the signal, measured as a composite mean magnitude of domain deformation and spin, μ.

We calculated confidence intervals[30] associated with the linear regressions for each of the elements of $\mathbf{L_T}$. We summarized the mean absolute value of these as a single confidence value e_T, which has the same units of proportion per minute as $\mathbf{L_T}$. We similarly summarized the amount of deformation and spin in $\mathbf{L_T}$ as μ_T, the mean absolute value of its four elements. In our example domain (**Fig. 3e**), $\mu_T = 0.0079$ and $e_T = 0.0053$, showing that there was both strong signal and strong inhomogeneity within the domain, which can be seen in the velocity field (**Fig. 3d**).

We explored the effect of varying n_c and dt on μ_T and e_T in our three example tissues (**Supplementary Fig. 2a–c**). We required domain sizes small enough to capture morphogenetic detail but large enough to have good signal-to-noise ratios. Increasing either n_c or dt reduced μ_T and e_T in all three tissues. There was greatest reduction of e_T from $n_c = 1$ to $n_c = 2$, whereas μ_T reduced from $n_c = 1$ to $n_c = 2$ but was then stable. We therefore selected $n_c = 2$ for all three example tissues. Similarly, μ_T and e_T stabilized at $dt = 1$ min for the *Drosophila* germband and $dt = 4$ min for the other two examples, and we used these settings throughout the paper.

We calculated a standard error, e_C, for the distribution of individual cell shape deformations within each domain, of which

$\dot{\mathbf{E}}_C$ was the mean. We also calculated the strength of cell shape deformation, μ_C, as the mean absolute value of the elements of $\dot{\mathbf{E}}_C$. In our example domain (**Fig. 3g**), $\mu_C = 0.0039$ and $e_C = 0.0031$, which showed a weaker cell shape signal compared to the tissue measure, whereas the error was proportionately larger. The distribution of e_C for each example tissue is shown (**Supplementary Fig. 2d–f,g**).

$\mathbf{L}_I$ is the most derived of our three strain rate measures, dependent on both cell centroid and cell shape measures being accurate and consistent (equation 1). The dilatation rate (rate of area change) of $\mathbf{L}_I$ should be zero but in practice this is not guaranteed. Differences in the dilatation rates of $\mathbf{L}_T$ and $\mathbf{L}_C$ caused the dilatation rate of $\mathbf{L}_I$ to be nonzero. This can occur when gaps within domains, caused by missing cells, behave differently to included cells. For example, gaps may change shape, influencing $\mathbf{L}_T$, but not influencing $\mathbf{L}_C$. We used $e_I = |\text{trace } \mathbf{L}_I| / 2$ as a measure of intercalation error and defined intercalation signal, μ_I, as half the absolute difference between the eigenvalues derived from $\mathbf{L}_I$. In our example domain (**Fig. 3**), $\mu_I = 0.0085$ and $e_I = 0.00016$. The error was very low because the traces of $\mathbf{L}_T$ and $\mathbf{L}_C$ were very similar. The means of the distributions of e_I were small compared to those of μ_I (**Supplementary Fig. 2g**). We set an intercalation error threshold of 0.009 proportion min^{-1} above which domains were classified as being based on inconsistent $\mathbf{L}_C$ and $\mathbf{L}_I$ measures and were rejected from the analyses. This removed 0.1%, 3.2% and 5.5% of domains from our three example tissues, respectively.

Imaging morphogenesis in living tissues. Wild-type zebrafish (*Danio rerio*) and *Drosophila melanogaster* embryos with fluorescently-labeled cell membranes were imaged using three-dimensional time-lapse confocal microscopy. Transgenic wild-type *Drosophila* embryos carried an *ubiDECadherinGFP* construct[31] that expresses a fusion between DE-Cadherin and GFP, thus labeling the apical cell outlines. Dechorionated embryos were covered with Voltalef oil 10S (Attachem) and viewed with an ×40 oil immersion Plan/Fluor (numerical aperture, NA = 1.3) objective. For imaging the *Drosophila* amnioserosa during dorsal closure, stage 14 (ref. 32) embryos were mounted on a coverslip with the dorsal side glued to the glass. A 50 min time-lapse movie, starting at the beginning of the zippering stage[17], was taken using an inverted LSM 510 Meta laser scanning microscope. 50 *z*-dimension sections 1 μm apart were collected every 2 min, with the whole of the amnioserosa in view (**Fig. 4a** and **Supplementary Video 1**). For the *Drosophila* germband, cellularised embryos were mounted ventral side up between an O₂-permeable membrane (Sartorius) and a coverslip using a custom-made frame for imaging on an upright Nikon Eclipse E800 microscope coupled to a MRC1024 Biorad confocal. Ten *z*-dimension sections 1 μm apart starting from the apical surface of the cells were taken every 30 s with the ventral and ventral-lateral cells of the extending germband in view (**Fig. 4i** and **Supplementary Video 2**).

For visualizing morphogenesis in the zebrafish, all cell membranes were rendered fluorescent by injecting a one-cell stage embryo with 230 pg of capped membrane-targeted mRNA generated from pCS2-fGFP (subcloned from Clontech pEGFP-F), linearized by *Not*I and transcribed using the MEGAscriptTM SP6 *in vitro* transcription kit (Ambion, Inc.). Live gastrulating embryos were mounted in a custom-made chamber in 0.3% low-gelling agarose and imaged dorsal side down on an inverted Leica Microsystems TSC-SP2-MP confocal microscope, using a long distance ×40 water immersion objective (NA = 0.8). 50 *z*-dimension sections every 2 μm were collected every 2 min (**Fig. 4q** and **Supplementary Video 3**).

Embryo layers and cell tracking. We sensed the shape of the surface of the embryo in each three-dimensional image stack[8] and used these shapes to extract curved image layers of constant radial depth within the embryo. Our methods for quantifying strain rates used distances and velocities calculated across the surface of such curved layers, taking into account the local inclination of the embryo. For *Drosophila* tissues we extracted layers through the apical *zonula adherens* of the ectoderm, the site at which much cell-cell interaction is controlled, and for zebrafish tissues we took a surface cutting through the middle of the outermost layer of epiblast cells. Repeating the analysis for different depths of tissues will identify whether the tissue is behaving homogenously in depth, or which layers deform first. The approximate angular curvature spanning an average domain of cells ($n_c = 2$) were 26.9, 13.3 and 9.0 degrees for our three example tissues, respectively. We wrote software to track all cells in these pseudo-two-dimensional layers over time (G.B.B. & R.J.A., unpublished data), based on the identification of the cell membranes (**Supplementary Videos 1–3** and **Fig. 4a,i,q**). The tracking software recorded for each valid cell, at each time point: the pixelated shape described by the fluorescent cell membrane and hence the cell area; the location of the cell centroid (center of mass); cell identity; the identity of all touching neighbors. We filtered out parts of tracked cell lineages that did not meet criteria for reasonable behavior, such as anomalously high rates of volume change or cell displacement compared to the immediate cell neighborhood. This removed 2.5%, 3.9% and 20.9% from our three example tissues respectively. Our analyses were designed to have the essential quality of being robust to occasional missing cells. All cells that touched the edge of the field of view are excluded from the analyses because they may have been incomplete. The average number of cells per time point used for strain rate analysis was 87, 522 and 503, respectively.

Multiple embryo alignment. We aligned 5 *Drosophila* and 9 zebrafish wild-type embryo movies in space and time, by co-aligning the embryonic midlines and locating a common developmental staging point along the AP direction in each movie. For the fly this was the location of the cephalic furrow 5 min after the start of germband extension, and for the fish trunk ectoderm, it was the location of the boundary between somites 1 and 2 when it first became visible (10.5 h after fertilization). The pooled embryos were broken down into 20 and 25 μm grid squares, in fly and fish, respectively, and average strain and rotation rates in each square were calculated.

28. Press, W.H., Flannery, B.P., Teukolsky, S.A. & Vetterling, W.T. *Numerical Recipes in C* (Cambridge University Press, Cambridge, UK, 1988).
29. Aubouy, M., Jiang, Y., Glazier, J.A. & Graner, F. A texture tensor to quantify deformations. *Granular Matter* **5**, 67–70 (2003).
30. Draper, N.R. & Smith, H. *Applied Regression Analysis* 3rd edition (John Wiley & Sons Inc., New York, 1998).
31. Oda, H. & Tsukita, S. Real-time imaging of cell-cell adherens junctions reveals that *Drosophila* mesoderm invagination begins with two phases of apical constriction of cells. *J. Cell Sci.* **114**, 493–501 (2001).
32. Campos-Ortega, J.-A. & Hartenstein, V. *The Embryonic Development of Drosophila melanogaster* (Springer-Verlag, Berlin, 1997).